ACS Catalysis

pubs.acs.org/acscatalysis

Research Article

Protein Conformational Change Is Essential for Reductive Activation of Lytic Polysaccharide Monooxygenase by Cellobiose Dehydrogenase

Erik Breslmayr, Christophe V. F. P. Laurent, Stefan Scheiblbrandner, Anita Jerkovic, Derren J. Heyes, Chris Oostenbrink, Roland Ludwig, Tobias M. Hedison,* Nigel S. Scrutton, and Daniel Kracher*

Cite This: *ACS Catal.* 2020, 10, 4842−4853

Read Online

ACCESS | Metrics & More | Article Recommendations | Supporting Information

ABSTRACT: Large-scale protein domain dynamics and electron transfer are often associated. However, as protein motions span a broad range of time and length scales, it is often challenging to identify and thus link functionally relevant dynamic changes to electron transfer in proteins. It is hypothesized that large-scale domain motions direct electrons through a FAD and a heme *b* cofactor of the fungal cellobiose dehydrogenase (CDH) enzymes to the type-II copper center (T2Cu) of the polysaccharide-degrading lytic polysaccharide monooxygenases (LPMOs). However, as of yet, domain motions in CDH have not been linked formally to enzyme-catalyzed electron transfer reactions. The detailed structural features of CDH, which govern the functional conformational landscapes of the enzyme, have only been partially resolved. Here, we use a combination of pressure, viscosity, ionic strength, and temperature perturbation stopped-flow studies to probe the conformational landscape associated with the electron transfer reactions of CDH. Through the use of molecular dynamics simulations, potentiometry, and stopped-flow spectroscopy, we investigated how a conserved Tyr99 residue plays a key role in shaping the conformational landscapes for both the interdomain electron transfer reactions of CDH (from FAD to heme) and the delivery of electrons from the reduced heme cofactor to the LPMO T2Cu. Our studies show how motions gate the electron transfer within CDH and from CDH to LPMO and illustrate the conformational landscape for interdomain and interprotein electron transfer in this extracellular fungal electron transfer chain.

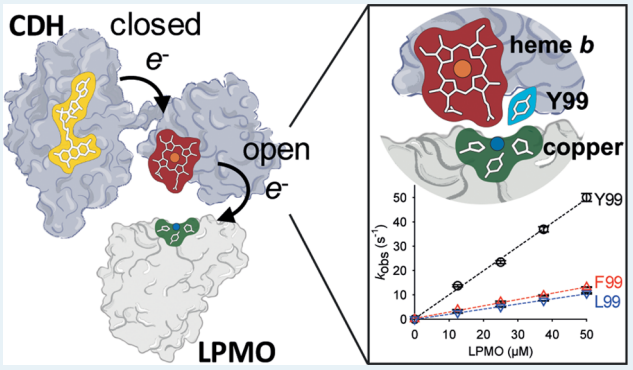

KEYWORDS: *protein dynamics, interdomain electron transfer, interprotein electron transfer, cellobiose dehydrogenase, domain movement, lytic polysaccharide monooxygenase*

INTRODUCTION

Protein conformational changes are often associated with enzyme catalysis[1,2] and, in many cases, they control and coordinate biological electron transfer reactions.[3−6] The fungal flavocytochrome cellobiose dehydrogenase [CDH; EC: 1.1.99.18; Carbohydrate Active enZYmes (CAZy; www.cazy.org) family: AA3_1] is an example of a dynamic redox enzyme that is thought to undergo large-scale structural changes in the transfer of electrons originating from a cellobiose substrate to a range of small molecules and proteinogenic redox partners.[7,8] At a structural level, CDH contains a mobile heme *b*-binding cytochrome (CYT) domain, which is tethered to a catalytic FAD-containing dehydrogenase (DH) domain via a flexible linker of varying length (15−35 amino acids).[9] During catalysis, the reduced FAD cofactor transfers electrons to the electron-accepting heme *b* cofactor (Figure 1A), which transfers electrons to extracellular redox partners.[10] Mechanistic studies have suggested that the delivery of electrons from the flavin to the heme cofactor and from the heme cofactor to external inorganic (e.g., quinoid) or proteinogenic electron acceptors is coordinated by motions of the CYT domain relative to the DH domain.[8] However, to date, motions have not been linked formally to the electron transfer processes of these enzymes. CDH is known to deliver electrons to fungal, cellulose-degrading and copper-containing lytic polysaccharide monooxygenases (LPMOs; EC 1.14.99.54, 1.14.99.56; CAZy family AA9).[8,10−13] Like many interprotein interactions, electron transfer between CDH and LPMO is thought to occur through the formation of a transient encounter

Received: February 13, 2020
Revised: March 30, 2020
Published: March 30, 2020

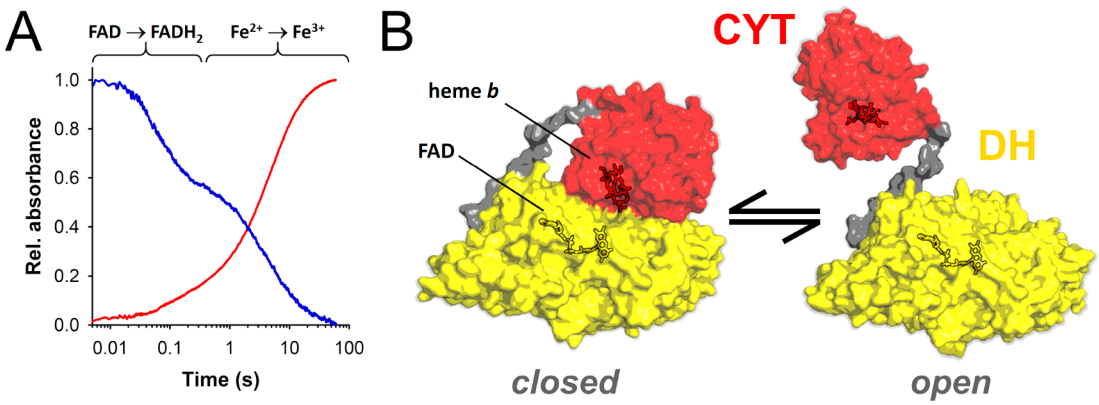

Figure 1. Electron transfer and conformational states of *Ch*CDH. (A) Exemplary stopped-flow traces of CDH, illustrating sequential electron transfer from the cellobiose substrate to the FAD and onward to heme *b*. Traces were obtained by mixing CDH (5 μM final concentration) with an excess of cellobiose (10 mM final concentration) and monitoring the quenching of the oxidized FAD isoalloxazine absorbance at 449 nm (blue trace) and growth of the heme *b* α-band at 563 nm (red trace). The second, slower phase measured at 449 nm is due to a partial overlap of FAD absorbance with the heme *b* Soret band. (B) Closed conformation of CDH illustrates the tight interaction of CYT and DH domains, in which the proximity of the cofactors allows electron transfer from the reduced FAD to heme *b* (PDB ID 4QI6). In the open conformation, both domains are physically separated from one another. This extended structure was obtained by modeling the sequence of *Ch*CDH onto the atomic structure of *Nc*CDHIIA in its fully open conformation (PDB ID 4QI7) using SWISS-MODEL (http://swissmodel.expasy.org/).[27]

complex.[14,15] AA9 LPMOs use O_2[16] or H_2O_2[17] as cosubstrate to catalyze the depolymerization of crystalline cellulose and hemicelluloses.[18] As they can be used to break down waste cellulose into fermentable sugars, LPMOs are key enzymes for the development of second-generation biofuels.[19]

Open and closed conformations of two full-length CDHs have been solved by X-ray crystallography.[10] These structures demonstrate that the enzyme occupies multiple conformational states (Figure 1B). The closed conformation seen in the crystal structure of CDH is characterized by a tight association of CYT and DH domains,[10] with the FAD and heme *b* cofactors separated by an 8.6 Å edge-to-edge distance. Such a conformation is thought to favor rapid electron transfer from the reduced FAD to the heme *b*. In the open conformation, the CYT and DH domains are separated (>50 Å edge-to-edge distance between the FAD and the heme *b*), with the CYT heme *b* occupying an orientation that is facing away from the DH domain (Figure 1B). Experimental[8,10,20] and computational[21] studies have demonstrated that these extended conformations allow interaction of the solvent-exposed, reduced heme *b* cofactor with proteinogenic electron acceptors (e.g., LPMO). Mechanistic insights from time-resolved spectroscopy of CDH and LPMO have confirmed a sequential electron transfer reaction that proceeds from the DH domain to the CYT domain[22−24] and onward from the CYT domain to the type-II copper center (T2Cu) present in LPMO.[10] They have also shown substantial differences between experimental and theoretical FAD to heme *b* electron transfer rates in CDH. A reaction rate of approximately 10^{10} s^{-1} would be expected based on free energy-minimized Moser−Dutton ruler measurements[25] in the closed conformation of the enzyme, but observed rate constants have been measured at 0.2−45 s^{-1} using stopped-flow spectroscopy,[10,22,26] suggesting that interdomain electron transfer is conformationally controlled and coordinated in CDH.

Solution-based structural approaches, including small-angle X-ray scattering (SAXS)[10,28] and small-angle neutron scattering (SANS),[28,29] have been used to study the solution structure of CDH. These studies complement crystallographic data and show that in solution, CDH samples a continuum of open and closed conformational states. Through the use of electrochemical[30,31] and kinetic[32] studies, it has been shown that surface electrostatics dictate the conformational landscape of the CDH and support the electron transfer chemistry catalyzed by the enzyme. Specifically, experimental data have indicated that in some CDHs, high concentrations of divalent cations enhance the rate of interdomain electron transfer reactions by masking the negative charges present at the interface between the two redox domains, shifting the conformational landscape of the enzyme to more closed conformations.[32] Hydrogen−deuterium exchange mass spectrometry (HDX-MS)[33] and SANS[29] have also shown that electrostatic repulsion of negatively charged patches on CDH modulates the interaction between the DH and the CYT domains. Taken together, these experiments provide strong evidence that the formation of electron transfer competent states during CDH catalysis, at least partially, relies on electrostatic steering. Substrate binding has also been shown to initiate conformational changes in CDH. A recent study employed time-resolved high-speed atomic force microscopy to show that binding of cellobiose initiated domain separation in CDH. This approach has also shown that the fully oxidized "substrate-free" CDH occupies a closed and static conformation.[7] However, to date, the link between domain motion and the reaction coordinate of CDH remains largely elusive. Moreover, key CDH residues, which shape the conformational landscape for functional interdomain and interprotein electron transfer states, are yet to be identified and characterized.

In this study, we use a range of solvent perturbation methods to access and probe the functional conformational landscape associated with the electron transfer reactions of CDH from *Crassicarpon hotsonii* (syn. *Myriococcum thermophilum*) (Figure 1B). Biophysical and computational approaches used here show that a conserved tyrosine residue models the conformational landscape of CDH by facilitating the interaction and the associated electron transfer chemistry between the DH and the CYT domain and the CYT domain with the LPMO partner protein. We demonstrate that domain mobility of CDH is essential in creating electron transfer competent states and show that a conserved amino acid (i.e.,

https://dx.doi.org/10.1021/acscatal.0c00754
ACS Catal. 2020, 10, 4842−4853

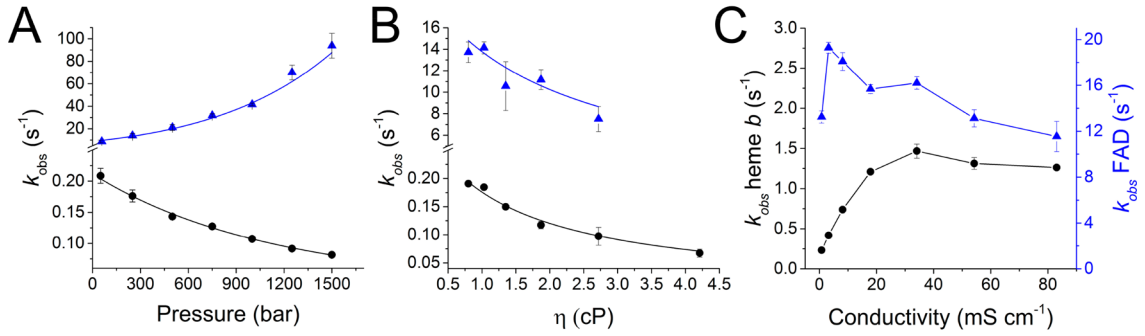

Figure 2. Electron transfer kinetics of CDH. (A) Effect of hydrostatic pressure on CDH-catalyzed FAD reduction (k_1, blue triangles) and intraprotein electron transfer (k_2, black circles). Data were fitted to eq 1 to calculate values for $\Delta V^{\ddagger}$ and $\Delta\beta^{\ddagger}$ (Table S1). (B) Effect of viscosity on CDH-catalyzed FAD reduction (k_1, blue triangles) and interdomain electron transfer (k_2, black circles). Data in B were fit to the Kramers equation (eq 2), and the corresponding friction coefficients (σ) and apparent Gibbs free energy values ($\Delta G^{\ddagger}$) are presented in Table 1. (C) Effect of ionic strength on CDH-catalyzed FAD reduction (k_1, blue triangles) and intraprotein electron transfer (k_2, black circles). Ionic strength-dependence stopped-flow measurements were performed by addition of potassium chloride (0−1 M) to the buffer. All experiments were performed in 50 mM sodium acetate buffer, pH 4.5, by mixing *Ch*CDH (5 μM final concentration) with cellobiose (5 mM final concentration) in a stopped-flow spectrometer. Each measurement was performed at least 3 times, and observed rate constants are presented ±1 SD.

Tyr99) located on the CYT domain of CDH is crucial for the function of these extracellular fungal lytic polysaccharide monooxygenase electron transfer chains.

RESULTS AND DISCUSSION

Conformational Landscapes and CDH Catalysis. To probe the functional relevance of protein domain dynamics in the electron transfer reactions of CDH from *C. hotsonii* (*Ch*CDH), we used a number of solvent perturbation methods (Figures 2 and S1). Hydrostatic pressure can be used to shift the conformational ensemble of a protein to more compact states that occupy smaller volumes and, in recent years, it has proven to be a useful method to identify and study functionally relevant protein domain dynamics.[3,5] In this study, to gain insight into pressure-induced structural changes of CDH, we first performed calculations on open and closed CDH conformations (Figure 1B) to determine the distribution of conformational states that would be favored under high-pressure conditions (Table S1). A maximal decrease in the surface area of 1961 Å^2 (or 6.7%) was obtained from the transition from the open to the closed conformation, reducing the number of water molecules interacting with *Ch*CDH by 152 (Figure 1B). Unless an increase in hydrostatic pressure leads to the population of conformational states that are catalytically incompetent, these closed conformations should support CDH-catalyzed intraprotein electron transfer reactions.

We studied FAD reduction (k_1) and intraprotein electron transfer (k_2) steps of *Ch*CDH by stopped-flow spectroscopy between atmospheric pressure (1 bar) and 1500 bar. Reactions were initiated by mixing *Ch*CDH (5 μM final concentration) with saturating concentrations of the substrate cellobiose (5 mM postmixing) to maintain pseudo-first-order conditions and followed by monitoring the decrease of the absorbance at 449 nm and the increase in the absorbance at 563 nm, representative of the FAD and heme reduction, respectively (Figure 1A). Observed rate constants across the pressure range used in our investigation are presented in Figure 2A. A substantial effect on both k_1 and k_2 was observed between 1 and 1500 bar. Specifically, over the pressure range measured, an approximately 10-fold increase and a 75% decrease in FAD reduction and FAD-to-heme electron transfer rates were seen, respectively. To quantitatively describe the trends from our high-pressure measurements, we fit the observed rate constants to eq 1

$$k_{obs}(p, T) = k_0 e^{(-\Delta V^{\ddagger} p/R_p T + \Delta\beta^{\ddagger} p^2/2R_p T)} \quad (1)$$

where the gas constant R_p is 83.14 cm^3 mol^{-1} bar K^{-1}, p is the pressure in bar, k_0 is the observed rate constant extrapolated to 0 bar, $\Delta V^{\ddagger}$ is the apparent difference between the volume of the reactant and transition states, and $\Delta\beta^{\ddagger}$ is the compressibility of the transition state: $\Delta\beta^{\ddagger} = d\Delta V^{\ddagger}/dp$.

For CDH-catalyzed flavin reduction, an activation volume ($\Delta V^{\ddagger}$) of −38.9 ± 8.6 cm^3 mol^{-1} at 25 °C was obtained. Other flavoenzymes, such as the members of the flavin-containing old yellow enzyme (OYE)[34] and the diflavin oxidoreductases[3,35] have previously been studied by high-pressure stopped-flow spectroscopy. In many of these investigations, pressure was shown to increase enzyme-catalyzed flavin reduction rates. Similarly, we observed pressure-dependent increases in the rate of CDH-catalyzed FAD reduction. We attribute these differences to lower activation volumes of the transition state for hydride transfer as pressure is increased.

Interdomain electron transfer showed a negative correlation with pressure and an activation volume of 17.6 ± 2.5 cm^3 mol^{-1} (Figure 2A and Table 1). As the expectation is that electron transfer distances would decrease with pressure, this result is counterintuitive. However, it can be rationalized by pressure-induced restriction of the conformational landscape

Table 1. Solvent Perturbation Stopped-Flow Fit Parameters

parameters	FAD reduction (k_1)	heme b reduction (k_2)
	pressure	
$\Delta V^{\ddagger}$ (cm^3 mol^{-1})	−38.9 ± 8.6	17.6 ± 2.5
$\Delta\beta^{\ddagger}$ (cm^3 mol^{-1} kbar^{-1})	−4.8 ± 10.7	3.7 ± 2.5
	solvent viscosity	
$\Delta G^{\ddagger}$ (303.15 K) (kJ mol^{-1})	61.6 ± 0.9	71.6 ± 0.4
σ (cP)	1.89 ± 0.9	1.17 ± 0.3
	temperature	
$\Delta G^{\ddagger}$ (303.15 K) (kJ mol^{-1})	68.4 ± 0.1	77.6 ± 0.1
ΔH (kJ mol^{-1})	23.5 ± 1.3	28.8 ± 1.1
ΔS (J mol^{-1} K^{-1})	−148.5 ± 4.5	−161.1 ± 3.8
ΔC_p (kJ mol^{-1} K^{-1})	−0.05 ± 0.14	−2.04 ± 0.2

https://dx.doi.org/10.1021/acscatal.0c00754
ACS Catal. 2020, 10, 4842−4853

that disfavors population of geometries required for optimal electron transfer. Conformational sampling across the landscape is required to transiently reduce the distance between the donor and the acceptor redox cofactors in order to maximize electronic coupling for the electron transfer reaction. This equilibrium will be affected by pressure modulation of the protein landscape. Other multidomain electron transfer systems (e.g., the calmodulin-free nitric oxide synthase,[35] cytochrome P450 reductase[3]), in which electron transfer reactions are facilitated by large-scale protein motions, have shown a similar pressure-dependent effect on the rates of interdomain electron transfer. Conformational sampling models for interdomain electron transfer in which observed rates of electron transfer are limited by the ability to explore the protein landscape are common in biology.[36] Electron transfer in CDH is therefore consistent with this trend.

To further probe the effect of domain mobility on intraprotein electron transfer in CDH, we performed solvent viscosity-dependent stopped-flow spectroscopic measurements (Figure 2B). Modulating the viscosity of the bulk solvent is a well-established method of probing the role of large-scale protein domain motions in catalysis.[3,37,38] Here, we used a range of glycerol concentrations (0−50%) to alter solvent viscosity and performed stopped-flow measurements between 0.75 and 4.25 cP to probe the interdomain electron transfer. In Figure 2B, observed rate constants as a function of viscosity are presented. To determine the friction coefficients (σ) of these CDH-catalyzed electron transfer reactions, trends were fit to the Kramers model (eq 2)

$$k_{obs} = \frac{k_0 T}{h}\left(\frac{1+\sigma}{\sigma+\eta}\right)e^{-\Delta G^{\ddagger}/RT} \quad (2)$$

where η is the solution viscosity, $\Delta G^{\ddagger}$ is the Gibbs free energy, and σ denotes the contribution of the protein friction to the total friction of the system.

Both k_1 and k_2 decreased when the viscosity of the solvent was increased (Figure 2B). It must be noted that solvent viscosities above 3 cP were accompanied by mixing effects, which caused up to 20 ms delay in our measurements. These effects interfered with the weak FAD signal and obscured accurate measurements of CDH-catalyzed FAD reduction at high glycerol concentrations. Friction coefficients (σ) and apparent Gibbs free energy ($\Delta G^{\ddagger}$) values for FAD reduction and intraprotein electron transfer are shown in Table 1. Gibbs free energy ($\Delta G^{\ddagger}$) values calculated from fits to the Kramers equation and from nonlinear Eyring fits (Equation S1) to temperature-dependent stopped-flow data (Table 1) are in agreement (temperature-dependent steady-state data shown in Figure S2). Of note, we observed significant curvature of Arrhenius-type fits of our temperature data (Figure S1). Such nonlinear behavior has been linked to vibrational changes in the protein structure, and respective negative $\Delta C_p^{\ddagger}$ values could be correlated to the dynamic behavior of enzymes.[39−41]

With a reduction in the rate of intraprotein electron transfer (k_2, Figure 2B), the solvent viscosity stopped-flow findings are consistent with the notion that large-scale domain motions accompany the intraprotein electron transfer reaction of CDH. Structural data have shown that the binding of the substrate analogue cellobiono-1,5-lactam induced only minor alterations in the active site geometry,[10] suggesting a similar situation for the native, β-1,4-linked substrate cellobiose. Our observations suggest that long-range dynamical motions from the bulk solvent through the protein entrance channel to the DH active site might influence the rate of FAD reduction in CDH. Similar effects have been seen with other enzymes where crystallography has identified a relatively rigid active site structure.[42] However, we must note that the influence of glycerol on the FAD reduction rate may be at least partially attributed to competition between glycerol and the cellobiose substrate. The strict dependence of the observed intraprotein electron transfer rates on solvent viscosity observed in our experiments provides evidence that prior to reduction, the CDH domains are not optimally arranged to enable rapid electron transfer and that extensive remodeling of the protein landscape through the relative motion of the CDH domains is required.

A number of studies have suggested that ionic strength might influence the conformational landscape of CDH by neutralizing charged amino acids and bridging the DH and CYT domains.[28,43] To investigate how ionic strength influences the kinetics of CDH-catalyzed FAD reduction and intraprotein electron transfer, we performed conductivity-dependent stopped-flow kinetics experiments on CDH by adding up to 1 M of potassium chloride to buffered solutions. Ionic strength stopped-flow data presented in Figure 2C show that intraprotein electron transfer reaction rates increased approximately 6-fold, while the FAD reduction rates decreased slightly as the concentration of potassium chloride in the buffered solutions was increased up to 1 M (Figure 2C). However, this beneficial effect of high potassium chloride concentrations was only seen in single-turnover stopped-flow reactions when mixing cellobiose with CDH; the steady-state turnover rates of CDH were only moderately influenced when using the electron acceptors cytochrome *c* and DCIP (Figure S3). These observations are consistent with a high ion concentration favoring more compact conformations of the enzyme, which favor intraprotein electron transfer. In contrast, the open (more extended) conformations of the enzyme are required for efficient CDH-to-LPMO or CDH-to-small molecule electron transfer reactions.

Combined, pressure, solvent viscosity, and ionic strength stopped-flow measurements show how protein motions are important for coordinating intraprotein electron transfer in CDH. While many studies have shown that CDH is highly dynamic, the data presented here show for the first time that electron transfer and CDH domain motions are inextricably linked. With this knowledge, we set out to identify structural features of CDH that are crucial in forming productive interdomain and interprotein electron transfer geometries.

Conserved Tyrosine Is Crucial for Functional Domain Motions and Interaction with LPMO. Our solvent and pressure perturbation stopped-flow data imply a role of protein domain dynamics in CDH-catalyzed electron transfer reactions. However, the structural features of CDH that support conformational sampling required for electron transfer are largely unknown. Here, we set out to identify conserved CDH amino acids that facilitate the electron transfer by forming productive interdomain and interprotein electron transfer geometries.

A number of amino acid residues that line the surface of the DH domain have previously been implicated in facilitating intraprotein electron transfer.[10] Direct experimental demonstration of the role of these residues in support of electron transfer from CDH to LPMO has been challenging. Experimental[10,20,28] and computational[21] studies have indicated that electron transfer between CDH and LPMO depends

https://dx.doi.org/10.1021/acscatal.0c00754
ACS Catal. 2020, 10, 4842−4853

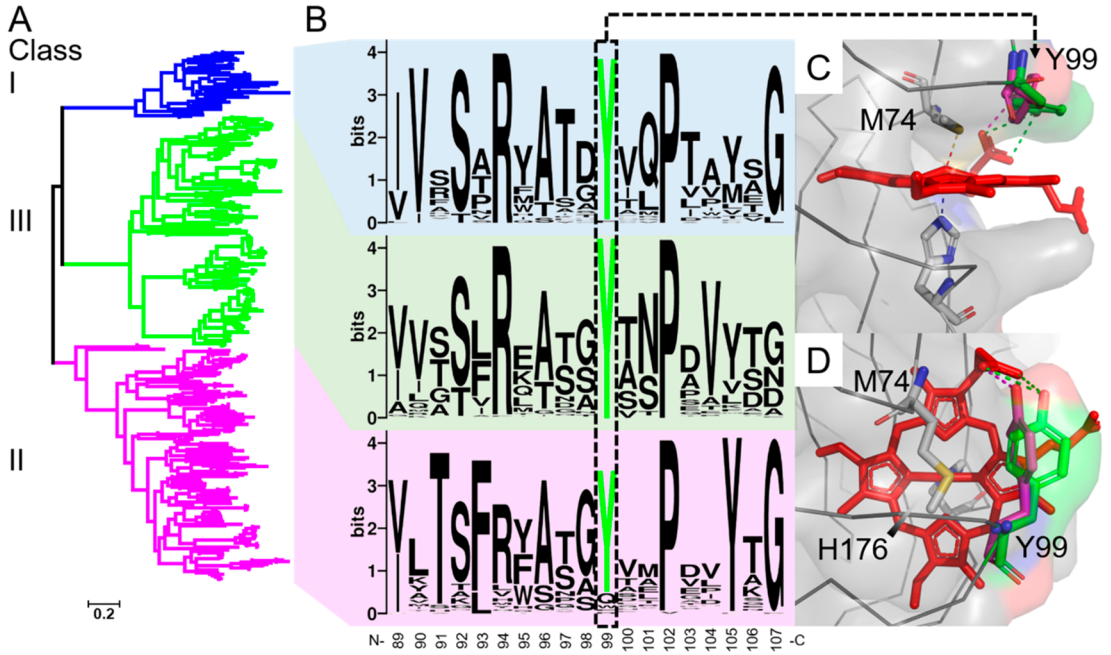

Figure 3. Conservation of Tyr99 in different CDH classes. (A) Phylogenetic analysis of 365 *cdh* sequences showing the known partition of CDHs into Class I (from Basidiomycete fungi), Class II (from Ascomycete fungi), and the yet uncharacterized Class III CDHs (from Ascomycete fungi). Existence of Class IV CDHs was recently reported[45] but was omitted in this analysis since members of this class do not contain a CYT domain. (B) Sequence logos illustrating the conservation of Tyr99 in the CDH classes. Numbering is according to *Ch*CDH. (C and D) Front- and top view, respectively, of the crystal structure of *Ch*CDH in the closed conformation (PDB ID 4QI6) showing the position of Tyr99 (green). For comparison, the conformation of Tyr99 in the isolated, crystallized CYT domain of *Ch*CDH (PDB ID 4qi3) is shown in pink. Dotted green and pink lines indicate polar interactions with the heme propionate D.

Table 2. Electrochemical and Kinetic Properties of *Ch*CDH Variants[a]

				+375 mM KCl		no KCl		
variant	$E°$ (mV vs SHE)	J'^{a} (μA cm^{-2})	cyt *c*, k_{cat} (s^{-1})	k_2 (s^{-1})	k_1 (s^{-1})	k_2 (s^{-1})	k_1 (s^{-1})	IPET (M^{-1} s^{-1})
*Ch*CDH	141	2.51	0.51 ± 0.01	1.47 ± 0.09	13.8 ± 1.1	0.17 ± 0.01	13.6 ± 0.3	9.87×10^5
Tyr99Phe	152	1.28	0.12 ± 0.01	0.43 ± 0.02	14.3 ± 0.2	0.12 ± 0.01	14.4 ± 0.2	2.58×10^5
Tyr99Leu	133	0.89	0.11 ± 0.01	0.25 ± 0.01	13.2 ± 0.3	0.10 ± 0.01	13.6 ± 0.3	2.10×10^5

[a]$E°$, electrochemical midpoint potentials of the heme *b* cofactors. *J*, current densities. cyt *c*, cytochrome *c*. k_1, FAD reduction. k_2, intraprotein electron transfer between the $FADH_2$ and heme *b* cofactors. IPET, interprotein electron transfer between heme *b* and *Nc*LPMO9C. Current densities at 250 mV vs SHE after subtraction of the capacitive current (blank).

on a direct interaction between the heme *b* present in the CYT domain and T2Cu present in the LPMO active site. In all studies to date, neither a role for surface complementarity nor electrostatic interactions have been demonstrated in guiding the interaction between CDH and LPMO. A conserved amino acid on the CYT domain that might interact with LPMO is a tyrosine residue (Tyr99 in *Ch*CDH),[21] which also forms polar contacts to the propionate D arm of the heme *b*.[10,44] Possible interaction partners of Tyr99 on the DH domain have not yet been identified.[21] In the closed conformations of CDH, Tyr99 is in close proximity (4.3 Å) to Arg698, which interacts with the heme *b* propionate A. This distance would allow bonding and/or π-cation interactions in the closed conformations of the enzyme. Importantly, Arg698 has been shown to be essential for CDH-catalyzed intraprotein electron transfer.[10]

A phylogenetic analysis of 362 *cdh* sequences derived from Ascomycete and Basidiomycete fungi showed high conservation of the tyrosine in all phylogenetically distinct CDH classes (Figures 3 and S4). This points toward a potentially important role for Tyr99 in electron transfer. Amino acids flanking the tyrosine were less conserved, except for Pro102 and Tyr105 (numbering for *Ch*CDH), both of which are not located in the vicinity of the porphyrin ring. These residues might fulfill other structural roles. We note that a small subset of sequences contained amino acids other than tyrosine at the *Ch*CDH position 99. Class IIA CDHs showed the highest variation: a distinct phylogenetic clade comprising sequences from *Oxysporium* sp. (3.8% of all sequences) contained glutamine, while in other sequences, the tyrosine was replaced by phenylalanine, tryptophan, or arginine (2.5% of all sequences). To date, none of these CDHs have been expressed or biochemically characterized.

We used site-directed mutagenesis to interrogate the role of Tyr99 in *Ch*CDH-catalyzed interdomain and interprotein electron transfer. To eliminate polar contacts to the propionate D, Tyr99 was replaced by phenylalanine. In addition, the aromatic functionality at this position was removed by creating a Tyr99Leu variant. The UV−vis absorption features of these variants were identical to those of the wild-type enzyme, indicating that the mutations had not compromised the binding or coordination of heme *b* (Figure S5A). All enzymes retained activity, as indicated by the typical shift of the CDH Soret band when the enzyme was reduced with cellobiose (Figure S5B). Steady-state kinetic measurements with the

https://dx.doi.org/10.1021/acscatal.0c00754
ACS Catal. 2020, 10, 4842−4853

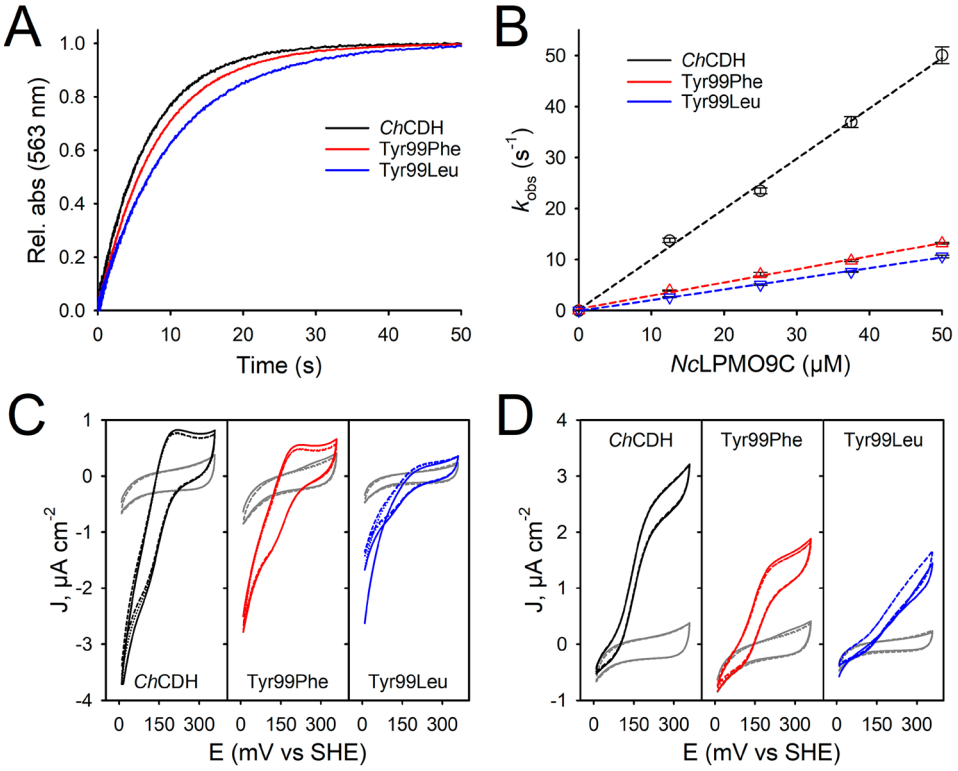

Figure 4. Stopped-flow traces and potentiometric measurements of *Ch*CDH variants. (A) Interdomain electron transfer between $FADH_2$ and heme *b* in CDH was measured by mixing CDH (5 μM final concentration) with cellobiose (5 mM final concentration) under anaerobic conditions. Absorbance values were normalized to 1 for better comparison. Reactions were performed in 50 mM sodium acetate buffer, pH 4.5, at 30 °C. (B) Interprotein electron transfer between *Ch*CDH variants and *Nc*LPMO9C was measured by mixing stoichiometrically reduced CDH (10 μM) with varying concentrations of LPMO. Kinetic traces are shown in Figure S7. All reactions were carried out in 50 mM sodium acetate buffer, pH 4.5, under anaerobic conditions at 30 °C. (C) Cyclic voltammograms of CDH variants immobilized on thiol-modified gold electrodes. Shown are the first three scans indicated by a dotted line, dashed line, and solid line. Capacitive currents of the electrodes in the absence of enzymes are shown in gray. Data were recorded at pH 4.5 in 50 mM sodium acetate buffer at a scan speed of 10 mV s^{-1}. (D) Catalytic currents obtained in the presence of 20 mM cellobiose.

commonly used heme *b*-dependent electron acceptor cytochrome *c* indicated that variants retained the same pH-dependent profile as the wild-type enzyme but had lower (~75%) specific activities (Table 2, Figure S6A). The reduction of the DH-specific electron acceptor 2,6-dichlorindophenol (DCIP) was also not affected in the variant enzymes (Figure S6B).

We used stopped-flow spectroscopy to study the intraprotein electron transfer reaction in the CDH variants by mixing oxidized CDH with saturating concentrations of cellobiose to maintain pseudo-first-order conditions (Figure 4A). A decrease in k_2 ($FADH_2$ to heme electron transfer rates) was measured for both Tyr99 variants (~29% and 41% reduction for the Phe and Leu variant, respectively). This effect was substantially increased in the presence of 375 mM potassium chloride, with a 71% and 83% reduction in the observed rates of intraprotein electron transfer for the Tyr99Phe and Tyr99Leu variants, respectively. Observed FAD reduction rates remained the same as the wild-type enzyme in both variants (Table 1). As midpoint potentials for the heme *b* cofactor were essentially identical in the wild type and the variants (Table 2), these differences in intraprotein electron transfer rates in the variant enzymes were not attributed to alterations in the redox driving force. Instead, our results point to a role of Tyr99 in forming productive geometries for CDH-catalyzed intraprotein electron transfer reactions. As there is a similar effect on intraprotein electron transfer rates in both variants, we suggest that hydrogen bonding between the hydroxyl moiety of the tyrosine residue and the heme propionate D arm is essential for positioning of the tyrosine residue and the heme cofactor for interactions with residues present in the DH domain (i.e., Arg698). Moreover, as the presence of KCl in our stopped-flow investigation enhances the mutational effect, we hypothesize that Tyr plays a key role in the electrostatic network between the DH and the CYT domains essential for productive intraprotein electron transfer.

Next, we probed the role of Tyr99 in interprotein electron transfer reactions from CDH to LPMO (Figure 4B and S7). To this end, we prereduced CDH with the substrate cellobiose and studied the kinetics of interprotein electron transfer by monitoring the reoxidation of 1-electron-reduced CDH when mixed with excess LPMO. The following interaction studies were performed in the absence of O_2, which can compete with CYT for electrons at the DH domain.[46] We observed that rate constants associated with interprotein electron transfer were linearly dependent on the LPMO concentration. These data imply that electron transfer from CDH to LPMO occurs through transient protein−protein interaction. Interprotein electron transfer rates from the CDH variants were approximately 4 times lower than those of the wild-type enzyme (second-order rate constant of 9.9×10^5 M^{-1} s^{-1}), with Tyr99Phe (2.6×10^5 M^{-1} s^{-1}) catalyzing interprotein

https://dx.doi.org/10.1021/acscatal.0c00754
ACS Catal. 2020, 10, 4842−4853

electron transfer slightly more efficiently than Tyr99Leu (2.1×10^5 M^{-1} s^{-1}).

Electrochemical analysis of the wild-type and variant enzymes by cyclic voltammetry showed a peak separation of ~65 mV for all investigated enzymes, demonstrating a quasi-reversible redox behavior (Figure 4C). Upon addition of cellobiose, catalytic currents were observed for all variants, demonstrating direct electron transfer to the electrode (Figure 4D). However, the lower current densities obtained with Tyr99Phe and Tyr99Leu indicate that the electron transfer to the electrode was negatively affected by replacement of the tyrosine. These data confirm a decreased electron transfer capacity of the variant enzymes, with Tyr99Phe yielding slightly higher current densities than Tyr99Leu. As the changes in the electron transferring capabilities are not attributed to differences in redox driving forces (Figures 4A and S8, Table 2), we suggest that Tyr99 plays a key role in forming productive interprotein electron transfer geometries and/or interactions. We observed that maintenance of an aromatic functionality (as in Tyr99Phe) at this position is not sufficient to promote efficient electron transfer. Therefore, we surmise that the polar contacts between the hydroxyl group of Tyr99 and the heme *b* propionate D are important for the orientation of the amino acid and/or the heme *b* cofactor for successful electron transfer to the LPMO protein.

Hydrogen Bonding between the Conserved Tyrosine and the Heme Cofactor Is Essential for Intra- and Interprotein Electron Transfer. Our data points to a role of a conserved tyrosine residue (Tyr99 in *Ch*CDH) in CDH-catalyzed intra- and interprotein electron transfer reactions and suggests hydrogen bonding between the conserved Tyr99 and the heme *b* is essential for positioning of the Tyr and/or the heme cofactor in an orientation that supports domain−domain and protein−protein interactions for efficient intra- and interprotein electron transfer. To probe possible interactions between Tyr99 and amino acids on the DH domain, we performed molecular dynamics (MD) simulations of the closed conformation of *Ch*CDH (PDB ID: 4QI6). Hydrogen bonds were calculated by considering the oxygen and hydrogen atoms of the Tyr99 hydroxyl group as hydrogen acceptor and donor, respectively. Three root-mean-square deviation (RMSD)-based clusters observed in a 50 ns simulation are shown in Figure S9 and highlight the observed hydrogen bonds. Hydrogen bonds between Tyr99 and both oxygen atoms of the heme propionate D occurred during 78.2% and 47.4% of the MD simulation time. In addition, hydrogen bonds between Tyr99 and the two terminal nitrogen atoms in the guanidium group of Arg698 were formed during the MD simulation 42.6% and 22.8% of the time. These data indicate that a hydrogen-bonding network supports the closed conformation of CDH. The inability of the Tyr99Phe and Tyr99Leu variants to form polar contacts to both the heme *b* and the Arg698 may destabilize the closed conformation. In the case of replacement by the smaller Tyr99Leu, additional water molecules could occupy the interaction surface and potentially decrease the interaction surface of the DH and CYT domain.

Next, we performed MD simulations on the isolated CYT domain of CDH to probe how the interaction between Tyr99 and the heme supports the positioning of the heme and the tyrosine residue for functional interdomain/interprotein interactions and thus catalysis. The mobility of residue 99 was examined when it was mutated to Phe and Leu. We mapped the relative mobility of Tyr99 along with the Phe and Leu replacements in an MD simulation performed for 50 ns. Figure 5A shows the relative mobility of each side-chain atom

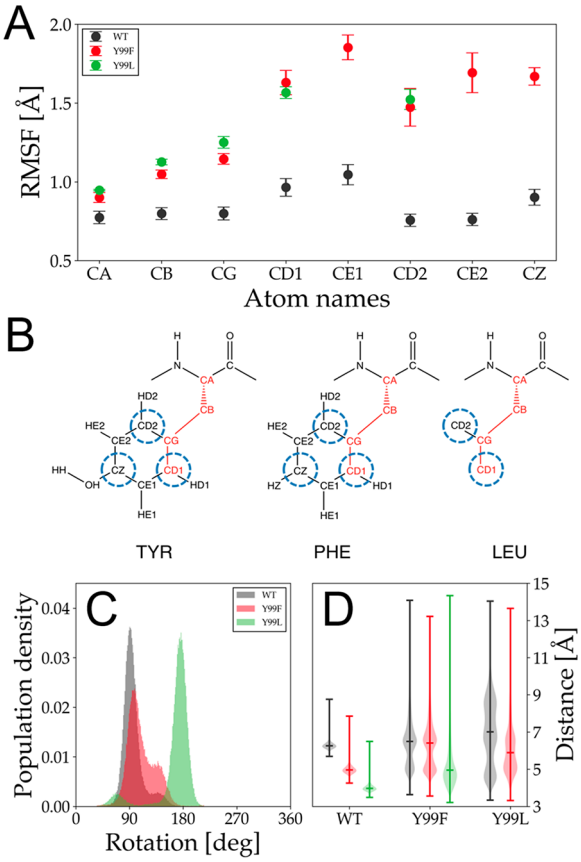

Figure 5. Analysis of molecular dynamics simulations. (A) Mean and standard error of the mean of the root-mean-square fluctuations (RMSF) of the *Ch*CDH variants (n = 3 independent simulations). (B) Overview of the atom name designations of tyrosine, phenylalanine, and leucine as used in the GROMOS force field.[47] Atoms used for measurement of the dihedral angles and distances shown in Figure 5A are highlighted in red and surrounded by blue circles, respectively. (C) Histograms of the rotation around an axis going through the atoms CB and CG of each variant. Rotations were measured by a dihedral angle described by atoms CA-CB-CG-CD1. (D) Violin plots of the distance between the atoms CD1 (black), CD2 (red), and CZ (green) and the carbon atom of the heme *b* propionate D carboxylic group.

in Tyr99, Phe99, and Leu99, illustrated by the root-mean-square fluctuation (RMSF). The atom designations are given in Figure 5B. For both variant enzymes, the RMSF of individual atoms increased significantly with increasing distance from the backbone chain. This reflects the higher mobility of the replaced amino acids relative to the wild-type enzyme, suggesting that the hydroxyl moiety positions Tyr99 in a fixed conformation. The importance of the hydrogen bond between the tyrosine hydroxyl group and the heme *b* propionate D was also reflected by the occurrence of this hydrogen bond during the MD simulations of the wild-type *Ch*CYT. A hydrogen bond could be observed in 99.8 ± 0.2% of the simulation in three independent MD simulations. By removing the hydroxyl group from Tyr99 in the Tyr99Phe variant, the polar contacts made to the heme *b* propionate D were disrupted. The dihedral angle distribution shown in Figure 5C indicates a preferred orientation of the aromatic ring

https://dx.doi.org/10.1021/acscatal.0c00754
ACS Catal. 2020, 10, 4842−4853

in Tyr99 with a maximum at 90° and a shoulder at around 140°. For Tyr99Phe, the dihedral angle distribution was shifted toward the minor peak observed for Tyr99. It has to be noted that these distributions are invariant to a 180° flipping of the aromatic residues. Therefore, the dihedral angles were manually shifted by plus or minus 180° to obtain a distribution in the range [0, 180°]. Flipping of these residues during the simulation was observed on average every 8.8 ns and every 10 ns for Tyr99Phe and Tyr99Leu, respectively. The dihedral angles for Tyr99Leu had a maximum at 180° and a smaller distribution around 70°, owing to its shorter chain length. These data are a strong indication that the interaction of Tyr99 with the heme *b* propionate D restricts the mobility of the amino acids and orients it in a defined manner. This is also reflected by distance measurements of defined atom positions in Tyr99 and the variant enzymes, which show that the aromatic ring of Tyr99 maintains a significantly lower distance to the heme *b* propionate D than the variant enzymes (Figure 5D). These data provide evidence that the interactions between the conserved Tyr99 and the heme *b* cofactor are important for interdomain (e.g., interactions between Tyr99 and Arg698) and interprotein interactions (directly from the heme/tyrosine to the T2Cu center) that are necessary to facilitate the electron transfer reactions of CDH.

CONCLUSIONS

Nature often uses multiple mechanisms to control and coordinate electron delivery to cofactors and substrates in redox proteins. Conformational, chemical, and ligand gating mechanisms are described in the literature and are used to control electron transfer reactions in important fundamental processes such as respiration, denitrification, photosynthesis, and drug detoxification. There is now strong evidence that cellobiose dehydrogenase (CDH) samples multiple conformational states in solution. Ligand binding and electrostatic interactions are known to facilitate conformational changes of CDH. However, how these structural changes influence the reaction chemistry has remained elusive. Likewise, the structural features of CDH that guide electron transfer from cellobiose to the lytic polysaccharide monooxygenase partner have remained unknown. Here, we provide compelling evidence that domain mobility facilitates electron transfer events in CDH. Stopped-flow studies with variable pressure, solvent viscosity, and ionic strength dependencies show how the protein landscape (i.e., open and closed states of CDH) is connected to intra- and interprotein electron transfer and how movement across this landscape facilitates electron transfer in these fungal LPMO electron transfer chains. Using computational methods in combination with electrochemical and kinetic measurements, we also pinpoint the importance of a conserved tyrosine residue (Tyr99 in *Ch*CDH), which is crucial for the interaction between the CYT domain and the DH domain as well as the interaction of the CYT domain with LPMO, its natural redox partner protein. Removal of the tyrosine influenced the electron transfer kinetics but not the redox potential of cofactors involved in this reaction. By hydrogen bonding to the heme cofactor, we conclude that the orientation of Tyr99 provides an important, albeit transient, interaction that facilitates both intra- and interprotein interactions required for the electron transfer chemistry. Our work, therefore, identifies important modulators and residues required for conformational sampling in CDH, which are necessary for the reductive activation of LPMOs by CDH, and it emphasizes the fundamental importance of dynamic protein structures in the control and coordination of long-range electron transfer in biology.

MATERIALS AND METHODS

Enzymes. Cellobiose dehydrogenase (CDH) from *Crassicarpon hotsonii* (*Ch*CDH, syn. *Myriococcum thermophilum*) was recombinantly produced in *Pichia pastoris* X-33 cells as described previously.[48] The variants Tyr99Phe and Tyr99Leu were generated by a two-step mutagenesis protocol using PCR and *Dpn*I, and correct nucleotide insertions were confirmed by gene sequencing. LPMO9C from *Neurospora crassa* (*Nc*LPMO9C) was expressed in *Pichia pastoris* X-33 and purified using previously published methods.[49] All enzymes were produced in a 4 L laboratory bioreactor (MBR, Switzerland) by following the *Pichia* Fermentation Process guidelines (Invitrogen). Protein expression was induced by applying an automated methanol feed, which was adjusted to maintain a constant dissolved oxygen concentration of 20%. The air flow rate was set to 6 L min^{-1}, the cultivation temperature was kept at 30 °C, and the stirrer speed was maintained at 800 rpm. Samples were taken on a daily basis and checked for enzyme activity and protein concentration. Enzyme purifications were done by hydrophobic interaction chromatography (PHE-Sepharose FF resin) followed by anion exchange chromatography (Source 15Q resin) using optimized protocols for *Ch*CDH[50] and *Nc*LPMO9C.[49] All purification steps were performed on an ÄKTA Pure FPLC system (GE Healthcare, Vienna, Austria). Purified enzymes were concentrated with centrifugal filters (Centricon; 10 kDa weight cutoff) to a concentration of approximately 20 mg mL^{-1} and stored at 4 °C.

Steady-State Activity Measurements. CDH was routinely assayed by following the cellobiose-dependent reduction of the electron acceptors cytochrome *c* (cyt *c*; ε_{550} = 19.6 $mM^{-1}\cdot cm^{-1}$) or dichloroindophenol (DCIP, ε_{520} = 6.9 $mM^{-1}\cdot cm^{-1}$). DCIP is reduced at the DH domain of CDH, while cyt *c* interacts selectively with the CYT domain of CDH.

Assays had a total volume of 1 mL and contained 20 μM cyt *c* or 300 μM DCIP in 50 mM sodium acetate buffer, pH 4.5. All reactions were conducted at 30 °C and contained 30 mM lactose as saturating substrate. Reactions were initiated by addition of 20 μL of enzyme solution. Absorbances were recorded over 180 s in a Lambda 35 spectrophotometer (PerkinElmer, Waltham, MA, USA) equipped with a thermocontrolled eight-cell changer. Enzyme activity was defined as the amount of enzyme that reduces 1 μmol of the respective electron acceptor per minute under the specified conditions.

Stopped-Flow Spectroscopy. Rapid kinetic measurements were performed with an SX-20 stopped-flow spectrophotometer (all equipment from Applied Photophysics, Leatherhead, UK) placed inside a Belle Technology anaerobic glovebox (<5 ppm of O_2). All reactions were carried out in 50 mM sodium acetate buffer, pH 4.5, which was kept in the glovebox overnight prior to all measurements to ensure removal of all oxygen traces. The redox state of the heme *b* cofactor was monitored at 563 nm (heme α band), while the FAD reduction was measured at 449 nm. Temperature- and salt-dependence measurements were performed using a constant enzyme concentration (5 μM final concentration) and a constant concentration of cellobiose (5 mM final concentration). Solvent viscosity measurements were per-

https://dx.doi.org/10.1021/acscatal.0c00754
ACS Catal. 2020, 10, 4842−4853

formed in the presence of glycerol at a constant temperature of 30 °C. Traces were fitted to exponential functions using the Pro Data software suite (Applied Photophysics). Observed rate constants are presented as an average of three measurements ±1 SD.

High-Pressure Stopped-Flow Spectroscopy. Fast kinetic reactions at high pressure were performed at 30 °C with a Hi-Tech Scientific HPSF-56 high-pressure stopped-flow spectrophotometer (TgK Scientific, Bradford on Avon, U.K.). All reactions were performed in 50 mM sodium acetate buffer, pH 4.5. Enzyme and cellobiose solutions were loaded into the reaction cells in an anaerobic glovebox. The final concentrations of CDH and cellobiose after mixing were 5 μM and 5 mM, respectively. Spectral changes accompanying FAD and heme *b* reduction were monitored at 449 and 563 nm, respectively. Rate constants were determined by fitting an exponential function to each trace. Rate constants were determined from at least 3 independent measurements and are presented ±1 SD.

Voltammetric Measurements. Cyclic voltammetry and square-wave voltammetry were performed on thiol-modified gold electrodes (diameter 1.6 mm; surface area 0.02 cm^2; BASi, West Lafayette, IN). The electrodes were prepared by immersing them in a piranha solution (H_2SO_4–H_2O_2 ratio of 3:1 [note that piranha solution is highly corrosive and can be explosive if hydrogen peroxide concentrations exceed 50%]) for 10 min, followed by electrochemical cleaning in 100 mM NaOH (between 0 and −1000 mV versus the standard hydrogen electrode (SHE) (10 cycles)). After polishing on Microcloth (Buehler, Lake Bluff, IL) in a Masterprep polishing suspension (0.05 μm; Buehler), the electrodes were sonicated for 10 min, followed by cycling in 0.5 M H_2SO_4 at a scan rate of 200 mV s^{-1} between 0 and +1950 mV versus SHE (20 cycles). Thiol self-assembled monolayer (SAM) formation at the electrode surfaces was done by immersing the electrodes in a 10 mM thioglycerol solution at room temperature (23 °C) overnight. The electrodes were covered with a Teflon cap to form a cell volume of about 30 μL. Modification with CDH was done by filling the cavity with enzyme solution (20 mg mL^{-1}). A dialysis membrane (molecular mass cutoff of 14 000 Da; Carl Roth) was used to trap the enzyme in the cells. Cyclic and square-wave voltammograms were recorded at room temperature (23 °C) at a scan rate of 10 mV s^{-1} between −50 and 350 mV versus SHE using a Gamry Reference 600 potentiostat (Gamry Instruments, Warminster, PA). The square-wave voltammograms were recorded at a frequency of 1 Hz, a step potential of 2 mV, and at an amplitude of 20 mV. A standard three-electrode configuration was used consisting of an AglAgCl reference electrode (saturated KCl; Gamry Instruments) and a platinum wire as a counter electrode. The buffer (50 mM sodium acetate, pH 4.5, containing 100 mM KCl) was degassed by purging the solution with argon prior to all experiments. During all measurements, argon was blown over the solution to maintain inert conditions.

Phylogenetic and Sequence Analysis. Sequence mining was done using the Hmmer algorithm *phmmer*[51] and applying the sequence from *Neurospora crassa* CDH IIB (GI 3874381) as a template. Hits were filtered by taxonomy and domain architecture, resulting in 362 putative CDH sequences (317 ascomycetous and 45 basidiomycetous sequences) containing the CDH–cytochrome motif (pfam PF16010) along with the GMC_oxred_N motif (pfam PF00732) or the GMC_oxred_C motif (pfam PF05199). Sequences without a cytochrome motif were omitted from the analysis. Among ascomycetous CDH sequences, 130 contained an additional type 1 carbohydrate-binding module (CBM1; pfam PF00734). Sequences were aligned using the ClustalO algorithm.[52]

Phylogenetic analysis of the derived multiple sequence alignment was performed using RAxML-NG (Randomized Axelerated Maximum Likelihood-Next Generation).[53] The best-fit substitution model for amino acid sequence "ModelTest-NG"[54] was used. For tree inference, the Wheelan and Goldman (WAG) model[55] with frequencies, invariant sited, and the number of gamma-distributed sites set to 4 was chosen, and 20 starting trees were calculated. A standard nonparametric bootstrap analysis was carried out until convergence criteria (cutoff 0.03) was reached based on the bootstopping test[56] (270 bootstraps). For branch support visualization the bootstrapped trees were mapped onto the best-scoring most likelihood tree on the original multiple sequence alignment.

Molecular Dynamics Simulations. All molecular dynamics (MD) simulations were performed with the GROMOS11 biomolecular simulation package.[57] The starting coordinates were taken from the crystal structure of the full-length *Ch*CDH (PDB ID 4QI6) or cytochrome domain of *Ch*CDH (PDB ID 4QI3). In order to create the coordinates for Tyr99Phe and Tyr99Leu, the respective atom coordinates were deleted from Tyr99 in *Ch*CYT. The GROMOS++ software package[58] with the GROMOS 54A7 force field[47] was used to parametrize all structures. Subsequently, a steepest descent energy minimization was performed using a convergence criterion of 0.1 kJ mol^{-1} with all of the parametrized structures. The SHAKE algorithm was used to constrain the bond lengths. The iron center of the heme *b* was ligated to its coordinating residues (i.e., and M74 S and H176 N_ε). After solvation with simple point charge (SPC) water[59] in a rectangular box with a minimal solute-to-wall distance of 0.8 nm, the structures were energy minimized once more to remove unfavorable solvent–solute interactions. To neutralize the total charge of the system, 34 sodium and 17 chloride atoms have been added by randomly replacing solvent molecules. Next, initial random velocities generated from a Maxwell–Boltzmann distribution were used to equilibrate the systems at 50 K. The temperature was then increased to 300 K during five discrete steps of 20 ps. The equilibration phase was repeated with three different seeds per variant. Finally, three plain MD production simulations were run for 50 ns per *Ch*CYT variant. To represent the medium outside the cutoff sphere, the reaction field method[60] was used to treat nonbonded interactions using a cutoff radius of 1.4 nm and an ε of 61. To maintain a constant temperature of 300 K and a constant pressure of 1 atm a weak coupling scheme with coupling times τ_T = 0.1 ps and τ_P = 0.5 ps and an isothermal compressibility of 4.575 × 10^{-4} kJ^{-1} mol nm^3 was used.[61] The subsequent trajectories were analyzed with the GROMOS++ software package, and the following python packages were used for data representation: NumPy (version 1.16.14)[62] and Matplotlib (version 3.1.0).[63] The PyMOL Molecular Graphics System (version 1.7.0.0, Schrödinger, LLC) was used to visualize and analyze the MD trajectories.

■ ASSOCIATED CONTENT

Supporting Information

This material is available free of charge on the ACS Publications Web site. The Supporting Information is available

https://dx.doi.org/10.1021/acscatal.0c00754
ACS Catal. 2020, 10, 4842−4853

free of charge at https://pubs.acs.org/doi/10.1021/acscatal.0c00754.

Solvent-accessible areas and water surface densities of *Ch*CDH; Arrhenius plots of steady- and presteady-state kinetic data; effect of the solvent conductivity on the steady-state turnover of CDH; multiple sequence alignment of CDH; UV−vis spectra of CDH variants; pH-dependent steady-state activities of *Ch*CDH, Tyr99Phe, and Tyr99Leu; kinetic traces of interprotein electron transfer between CDH and LPMO; square wave voltammograms of CDH variants; MD simulation of *Ch*CDH (PDF)

Full-length multiple sequence alignment of CDH sequences (Figure S4) (XLSX)

AUTHOR INFORMATION

Corresponding Authors

Tobias M. Hedison − *Manchester Institute of Biotechnology and EPSRC/BBSRC funded Future Biomanufacturing Research Hub, The Manchester Institute of Biotechnology, The University of Manchester, M1 7DN Manchester, United Kingdom*; Email: tobias.hedison@manchester.ac.uk

Daniel Kracher − *Manchester Institute of Biotechnology, The University of Manchester, M1 7DN Manchester, United Kingdom; Biocatalysis and Biosensing Laboratory, Department of Food Science and Technology, University of Natural Resources and Life Sciences, 1190 Vienna, Austria*; orcid.org/0000-0002-3856-3170; Email: danielkracher@boku.ac.at

Authors

Erik Breslmayr − *Manchester Institute of Biotechnology, The University of Manchester, M1 7DN Manchester, United Kingdom; Biocatalysis and Biosensing Laboratory, Department of Food Science and Technology, University of Natural Resources and Life Sciences, 1190 Vienna, Austria; Department of Material Sciences and Process Engineering, Institute of Molecular Modeling and Simulation, 1190 Vienna, Austria*

Christophe V. F. P. Laurent − *Biocatalysis and Biosensing Laboratory, Department of Food Science and Technology, University of Natural Resources and Life Sciences, 1190 Vienna, Austria; Department of Material Sciences and Process Engineering, Institute of Molecular Modeling and Simulation, 1190 Vienna, Austria*; orcid.org/0000-0002-9112-6981

Stefan Scheiblbrandner − *Biocatalysis and Biosensing Laboratory, Department of Food Science and Technology, University of Natural Resources and Life Sciences, 1190 Vienna, Austria*

Anita Jerkovic − *Biocatalysis and Biosensing Laboratory, Department of Food Science and Technology, University of Natural Resources and Life Sciences, 1190 Vienna, Austria*

Derren J. Heyes − *Manchester Institute of Biotechnology, The University of Manchester, M1 7DN Manchester, United Kingdom*

Chris Oostenbrink − *Department of Material Sciences and Process Engineering, Institute of Molecular Modeling and Simulation, 1190 Vienna, Austria*; orcid.org/0000-0002-4232-2556

Roland Ludwig − *Biocatalysis and Biosensing Laboratory, Department of Food Science and Technology, University of Natural Resources and Life Sciences, 1190 Vienna, Austria*; orcid.org/0000-0002-5058-5874

Nigel S. Scrutton − *Manchester Institute of Biotechnology and EPSRC/BBSRC funded Future Biomanufacturing Research Hub, The Manchester Institute of Biotechnology, The University of Manchester, M1 7DN Manchester, United Kingdom*; orcid.org/0000-0002-4182-3500

Complete contact information is available at: https://pubs.acs.org/10.1021/acscatal.0c00754

Notes

The authors declare no competing financial interest.

ACKNOWLEDGMENTS

This work was supported by the Austrian Science Fund (FWF) through grants J 4154-B32 (D.K.), W1224 (E.B., C.V.F.P.L., C.O., C.L.), the European Union's Horizon 2020 research and innovation programme (ERC Consolidator Grant OXIDISE) under grant agreement no. 726396 (S.S., R.L.), and the UK Biotechnology and Biological Sciences Research Council award BB/N013980/1 (T.M.H., D.J.H., N.S.S.). This work was supported by the Future Biomanufacturing Research Hub (grant EP/S01778X/1), funded by the Engineering and Physical Sciences Research Council (EPSRC) and Biotechnology and Biological Sciences Research Council (BBSRC) as part of UK Research and Innovation (T.M.H., N.S.S.).

ABBREVIATIONS

CDH, cellobiose dehydrogenase; LPMO, lytic polysaccharide monooxygenase; T2Cu, type-II copper center; CAZy, carbohydrate-active enzymes; CYT, cytochrome domain; DH, dehydrogenase domain; FAD, flavin adenine dinucleotide; SAXS, small-angle X-ray scattering; SANS, small-angle neutron scattering; DCIP, 2,6-dichloroindophenol; cyt *c*, cytochrome *c*; IPET, interprotein electron transfer between CDH and LPMO; MD, molecular dynamics; RMSD, root-mean-square deviation; RMSF, root-mean-square fluctuation

REFERENCES

(1) Henzler-Wildman, K. A.; Thai, V.; Lei, M.; Ott, M.; Wolf-Watz, M.; Fenn, T.; Pozharski, E.; Wilson, M. A.; Petsko, G. A.; Karplus, M.; Hübner, C. G.; Kern, D. Intrinsic Motions along an Enzymatic Reaction Trajectory. *Nature* **2007**, *450*, 838−844.

(2) Lerner, E.; Cordes, T.; Ingargiola, A.; Alhadid, Y.; Chung, S. Y.; Michalet, X.; Weiss, S. Toward Dynamic Structural Biology: Two Decades of Single-Molecule Förster Resonance Energy Transfer. *Science* **2018**, *359*, eaan1133.

(3) Hay, S.; Brenner, S.; Khara, B.; Quinn, A. M.; Rigby, S. E. J.; Scrutton, N. S. Nature of the Energy Landscape for Gated Electron Transfer in a Dynamic Redox Protein. *J. Am. Chem. Soc.* **2010**, *132*, 9738−9745.

(4) Leferink, N. G. H.; Pudney, C. R.; Brenner, S.; Heyes, D. J.; Eady, R. R.; Samar Hasnain, S.; Hay, S.; Rigby, S. E. J.; Scrutton, N. S. Gating Mechanisms for Biological Electron Transfer: Integrating Structure with Biophysics Reveals the Nature of Redox Control in Cytochrome P450 Reductase and Copper-Dependent Nitrite Reductase. *FEBS Lett.* **2012**, *586*, 578−584.

(5) Hedison, T. M.; Hay, S.; Scrutton, N. S. A Perspective on Conformational Control of Electron Transfer in Nitric Oxide Synthases. *Nitric Oxide* **2017**, *63*, 61−67.

(6) Hedison, T. M.; Scrutton, N. S. Tripping the Light Fantastic in Membrane Redox Biology: Linking Dynamic Structures to Function in ER Electron Transfer Chains. *FEBS J.* **2019**, *286*, 2004−2017.

(7) Harada, H.; Onoda, A.; Uchihashi, T.; Watanabe, H.; Sunagawa, N.; Samejima, M.; Igarashi, K.; Hayashi, T. Interdomain Flip-Flop Motion Visualized in Flavocytochrome Cellobiose Dehydrogenase

Using High-Speed Atomic Force Microscopy during Catalysis. *Chem. Sci.* **2017**, *8*, 6561−6565.
(8) Kracher, D.; Scheiblbrandner, S.; Felice, A. K. G.; Breslmayr, E.; Preims, M.; Ludwicka, K.; Haltrich, D.; Eijsink, V. G. H.; Ludwig, R. Extracellular Electron Transfer Systems Fuel Cellulose Oxidative Degradation. *Science* **2016**, *352*, 1098−1101.
(9) Sützl, L.; Laurent, C. V. F. P. F. P.; Abrera, A. T.; Schütz, G.; Ludwig, R.; Haltrich, D. Multiplicity of Enzymatic Functions in the CAZy AA3 Family. *Appl. Microbiol. Biotechnol.* **2018**, *102*, 2477−2492.
(10) Tan, T.-C.; Kracher, D.; Gandini, R.; Sygmund, C.; Kittl, R.; Haltrich, D.; Hällberg, B. M.; Ludwig, R.; Divne, C. Structural Basis for Cellobiose Dehydrogenase Action during Oxidative Cellulose Degradation. *Nat. Commun.* **2015**, *6*, 7542.
(11) Langston, J. A.; Shaghasi, T.; Abbate, E.; Xu, F.; Vlasenko, E.; Sweeney, M. D. Oxidoreductive Cellulose Depolymerization by the Enzymes Cellobiose Dehydrogenase and Glycoside Hydrolase 61. *Appl. Environ. Microbiol.* **2011**, *77*, 7007−7015.
(12) Phillips, C. M.; Beeson, W. T.; Cate, J. H.; Marletta, M. A. Cellobiose Dehydrogenase and a Copper-Dependent Polysaccharide Monooxygenase Potentiate Cellulose Degradation by *Neurospora Crassa*. *ACS Chem. Biol.* **2011**, *6*, 1399−1406.
(13) Loose, J. S. M. M.; Forsberg, Z.; Kracher, D.; Scheiblbrandner, S.; Ludwig, R.; Eijsink, V. G. H. H.; Vaaje-Kolstad, G. Activation of Bacterial Lytic Polysaccharide Monooxygenases with Cellobiose Dehydrogenase. *Protein Sci.* **2016**, *25*, 2175−2186.
(14) Bashir, Q.; Volkov, A. N.; Ullmann, G. M.; Ubbink, M. Visualization of the Encounter Ensemble of the Transient Electron Transfer Complex of Cytochrome *c* and Cytochrome *c* Peroxidase. *J. Am. Chem. Soc.* **2010**, *132*, 241−247.
(15) Crowley, P. B.; Ubbink, M. Close Encounters of the Transient Kind: Protein Interactions in the Photosynthetic Redox Chain Investigated by NMR Spectroscopy. *Acc. Chem. Res.* **2003**, *36*, 723−730.
(16) Quinlan, R. J.; Sweeney, M. D.; Lo Leggio, L.; Otten, H.; Poulsen, J.-C. N. J.-C. N.; Johansen, K. S.; Krogh, K. B. R. M.; Jørgensen, C. I.; Tovborg, M.; Anthonsen, A.; Tryfona, T.; Walter, C. P.; Dupree, P.; Xu, F.; Davies, G. J.; Walton, P. H. Insights into the Oxidative Degradation of Cellulose by a Copper Metalloenzyme That Exploits Biomass Components. *Proc. Natl. Acad. Sci. U. S. A.* **2011**, *108*, 15079−15084.
(17) Bissaro, B.; Røhr, Å. K.; Müller, G.; Chylenski, P.; Skaugen, M.; Forsberg, Z.; Horn, S. J.; Vaaje-Kolstad, G.; Eijsink, V. G. H. Oxidative Cleavage of Polysaccharides by Monocopper Enzymes Depends on H_2O_2. *Nat. Chem. Biol.* **2017**, *13*, 1123−1128.
(18) Walton, P. H.; Davies, G. J. On the Catalytic Mechanisms of Lytic Polysaccharide Monooxygenases. *Curr. Opin. Chem. Biol.* **2016**, *31*, 195−207.
(19) Beeson, W. T.; Vu, V. V.; Span, E. A.; Phillips, C. M.; Marletta, M. A. Cellulose Degradation by Polysaccharide Monooxygenases. *Annu. Rev. Biochem.* **2015**, *84*, 923−946.
(20) Courtade, G.; Wimmer, R.; Røhr, Å. K.; Preims, M.; Felice, A. K. G.; Dimarogona, M.; Vaaje-Kolstad, G.; Sørlie, M.; Sandgren, M.; Ludwig, R.; Eijsink, V. G. H.; Aachmann, F. L. Interactions of a Fungal Lytic Polysaccharide Monooxygenase with β-Glucan Substrates and Cellobiose Dehydrogenase. *Proc. Natl. Acad. Sci. U. S. A.* **2016**, *113*, 5922−5927.
(21) Laurent, C. V. F. P.; Breslmayr, E.; Tunega, D.; Ludwig, R.; Oostenbrink, C. Interaction between Cellobiose Dehydrogenase and Lytic Polysaccharide Monooxygenase. *Biochemistry* **2019**, *58*, 1226−1235.
(22) Igarashi, K.; Momohara, I.; Nishino, T.; Samejima, M. Kinetics of Inter-Domain Electron Transfer in Flavocytochrome Cellobiose Dehydrogenase from the White-Rot Fungus *Phanerochaete chrysosporium*. *Biochem. J.* **2002**, *365*, 521−526.
(23) Cameron, M. D.; Aust, S. D. Kinetics and Reactivity of the Flavin and Heme Cofactors of Cellobiose Dehydrogenase from *Phanerochaetechrysosporium*. *Biochemistry* **2000**, *39*, 13595−13601.
(24) Wilson, M. T.; Liu, B.-L. Electron Transfer Reactions of Cellobiose Oxidase. *Biochem. Soc. Trans.* **1994**, *22*, 725−728.
(25) Moser, C. C.; Keske, J. M.; Warncke, K.; Farid, R. S.; Dutton, P. L. Nature of Biological Electron Transfer. *Nature* **1992**, *355*, 796−802.
(26) Rogers, M. S.; Jones, G. D.; Antonini, G.; Wilson, M. T.; Brunori, M. Electron Transfer from Phanerochaete Chrysosporium Cellobiose Oxidase to Equine Cytochrome *c* and *Pseudomonas aeruginosa* Cytochrome C-551. *Biochem. J.* **1994**, *298*, 329−334.
(27) Waterhouse, A.; Bertoni, M.; Bienert, S.; Studer, G.; Tauriello, G.; Gumienny, R.; Heer, F. T.; De Beer, T. A. P.; Rempfer, C.; Bordoli, L.; Lepore, R.; Schwede, T. SWISS-MODEL: Homology Modelling of Protein Structures and Complexes. *Nucleic Acids Res.* **2018**, *46*, W296−W303.
(28) Bodenheimer, A. M.; O'Dell, W. B.; Oliver, R. C.; Qian, S.; Stanley, C. B.; Meilleur, F. Structural Investigation of Cellobiose Dehydrogenase IIA: Insights from Small Angle Scattering into Intra- and Intermolecular Electron Transfer Mechanisms. *Biochim. Biophys. Acta, Gen. Subj.* **2018**, *1862*, 1031−1039.
(29) Bodenheimer, A. M.; O'Dell, W. B.; Stanley, C. B.; Meilleur, F. Structural Studies of *Neurospora crassa* LPMO9D and Redox Partner CDHIIA Using Neutron Crystallography and Small-Angle Scattering. *Carbohydr. Res.* **2017**, *448*, 200−204.
(30) Schulz, C.; Ludwig, R.; Micheelsen, P. O.; Silow, M.; Toscano, M. D.; Gorton, L. Enhancement of Enzymatic Activity and Catalytic Current of Cellobiose Dehydrogenase by Calcium Ions. *Electrochem. Commun.* **2012**, *17*, 71−74.
(31) Kielb, P.; Sezer, M.; Katz, S.; Lopez, F.; Schulz, C.; Gorton, L.; Ludwig, R.; Wollenberger, U.; Zebger, I.; Weidinger, I. M. Spectroscopic Observation of Calcium-Induced Reorientation of Cellobiose Dehydrogenase Immobilized on Electrodes and Its Effect on Electrocatalytic Activity. *ChemPhysChem* **2015**, *16*, 1960−1968.
(32) Kracher, D.; Zahma, K.; Schulz, C.; Sygmund, C.; Gorton, L.; Ludwig, R. Inter-Domain Electron Transfer in Cellobiose Dehydrogenase: Modulation by pH and Divalent Cations. *FEBS J.* **2015**, *282*, 3136−3148.
(33) Kadek, A.; Kavan, D.; Felice, A. K. G.; Ludwig, R.; Halada, P.; Man, P. Structural Insight into the Calcium Ion Modulated Interdomain Electron Transfer in Cellobiose Dehydrogenase. *FEBS Lett.* **2015**, *589*, 1194−1199.
(34) Hay, S.; Sutcliffe, M. J.; Scrutton, N. S. Promoting Motions in Enzyme Catalysis Probed by Pressure Studies of Kinetic Isotope Effects. *Proc. Natl. Acad. Sci. U. S. A.* **2007**, *104*, 507−512.
(35) Sobolewska-Stawiarz, A.; Leferink, N. G. H.; Fisher, K.; Heyes, D. J.; Hay, S.; Rigby, S. E. J.; Scrutton, N. S. Energy Landscapes and Catalysis in Nitric-Oxide Synthase. *J. Biol. Chem.* **2014**, *289*, 11725−11738.
(36) Leys, D.; Scrutton, N. S. Electrical Circuitry in Biology: Emerging Principles from Protein Structure. *Curr. Opin. Struct. Biol.* **2004**, *14*, 642−647.
(37) Beece, D.; Eisenstein, L.; Frauenfelder, H.; Good, D.; Marden, M. C.; Reinisch, L.; Yue, K. T.; Reynolds, A. H.; Sorensen, L. B. Solvent Viscosity and Protein Dynamics. *Biochemistry* **1980**, *19*, 5147−5157.
(38) Fenimore, P. W.; Frauenfelder, H.; McMahon, B. H.; Parak, F. G. Slaving: Solvent Fluctuations Dominate Protein Dynamics and Functions. *Proc. Natl. Acad. Sci. U. S. A.* **2002**, *99*, 16047−16051.
(39) van der Kamp, M. W.; Prentice, E. J.; Kraakman, K. L.; Connolly, M.; Mulholland, A. J.; Arcus, V. L. Dynamical Origins of Heat Capacity Changes in Enzyme-Catalysed Reactions. *Nat. Commun.* **2018**, *9*, 1177.
(40) Arcus, V. L.; Pudney, C. R. Change in Heat Capacity Accurately Predicts Vibrational Coupling in Enzyme Catalyzed Reactions. *FEBS Lett.* **2015**, *589*, 2200−2206.
(41) Arcus, V. L.; Prentice, E. J.; Hobbs, J. K.; Mulholland, A. J.; Van der Kamp, M. W.; Pudney, C. R.; Parker, E. J.; Schipper, L. A. On the Temperature Dependence of Enzyme-Catalyzed Rates. *Biochemistry* **2016**, *55*, 1681−1688.

https://dx.doi.org/10.1021/acscatal.0c00754
ACS Catal. 2020, 10, 4842−4853

(42) Hedison, T. M.; Heyes, D. J.; Shanmugam, M.; Iorgu, A. I.; Scrutton, N. S. Solvent-Slaved Protein Motions Accompany Proton Coupled Electron Transfer Reactions Catalysed by Copper Nitrite Reductase. *Chem. Commun.* **2019**, *55*, 5863−5866.
(43) Kadek, A.; Kavan, D.; Marcoux, J.; Stojko, J.; Felice, A. K. G.; Cianférani, S.; Ludwig, R.; Halada, P.; Man, P. Interdomain Electron Transfer in Cellobiose Dehydrogenase Is Governed by Surface Electrostatics. *Biochim. Biophys. Acta, Gen. Subj.* **2017**, *1861*, 157−167.
(44) Hallberg, B. M.; Bergfors, T.; Bäckbro, K.; Pettersson, G.; Henriksson, G.; Divne, C. A New Scaffold for Binding Haem in the Cytochrome Domain of the Extracellular Flavocytochrome Cellobiose Dehydrogenase. *Structure* **2000**, *8*, 79−88.
(45) Sützl, L.; Foley, G.; Gillam, E. M. J.; Bodén, M.; Haltrich, D. The GMC Superfamily of Oxidoreductases Revisited: Analysis and Evolution of Fungal GMC Oxidoreductases. *Biotechnol. Biofuels* **2019**, *12*, 118.
(46) Kracher, D.; Forsberg, Z.; Bissaro, B.; Gangl, S.; Preims, M.; Sygmund, C.; Eijsink, V. G. H.; Ludwig, R. Polysaccharide Oxidation by Lytic Polysaccharide Monooxygenase Is Enhanced by Engineered Cellobiose Dehydrogenase. *FEBS J.* **2020**, *287*, 897−908.
(47) Schmid, N.; Eichenberger, A. P.; Choutko, A.; Riniker, S.; Winger, M.; Mark, A. E.; Van Gunsteren, W. F. Definition and Testing of the GROMOS Force-Field Versions 54A7 and 54B7. *Eur. Biophys. J.* **2011**, *40*, 843−856.
(48) Zámocký, M.; Schümann, C.; Sygmund, C.; O'Callaghan, J.; Dobson, A. D. W.; Ludwig, R.; Haltrich, D.; Peterbauer, C. K. Cloning, Sequence Analysis and Heterologous Expression in *Pichia pastoris* of a Gene Encoding a Thermostable Cellobiose Dehydrogenase from *Myriococcum thermophilum*. *Protein Expression Purif.* **2008**, *59*, 258−265.
(49) Kittl, R.; Kracher, D.; Burgstaller, D.; Haltrich, D.; Ludwig, R. Production of Four *Neurospora crassa* Lytic Polysaccharide Monooxygenases in *Pichia pastoris* Monitored by a Fluorimetric Assay. *Biotechnol. Biofuels* **2012**, *5*, 79.
(50) Martinez, A. T. How to Break down Crystalline Cellulose. *Science* **2016**, *352*, 1050−1051.
(51) Potter, S. C.; Luciani, A.; Eddy, S. R.; Park, Y.; Lopez, R.; Finn, R. D. HMMER Web Server: 2018 Update. *Nucleic Acids Res.* **2018**, *46*, W200−W204.
(52) Madeira, F.; Park, Y. mi; Lee, J.; Buso, N.; Gur, T.; Madhusoodanan, N.; Basutkar, P.; Tivey, A. R. N.; Potter, S. C.; Finn, R. D.; Lopez, R. The EMBL-EBI Search and Sequence Analysis Tools APIs in 2019. *Nucleic Acids Res.* **2019**, *47*, W636−W641.
(53) Kozlov, A. M; Darriba, D.; Flouri, T.; Morel, B.; Stamatakis, A. RAxML-NG: A Fast, Scalable and User-Friendly Tool for Maximum Likelihood Phylogenetic Inference. *Bioinformatics* **2019**, *35*, 4453−4455.
(54) Darriba, D.; Posada, D.; Kozlov, A. M.; Stamatakis, A.; Morel, B.; Flouri, T. ModelTest-NG: A New and Scalable Tool for the Selection of DNA and Protein Evolutionary Models. *Mol. Biol. Evol.* **2020**, *37*, 291−294.
(55) Whelan, S.; Goldman, N. A General Empirical Model of Protein Evolution Derived from Multiple Protein Families Using a Maximum-Likelihood Approach. *Mol. Biol. Evol.* **2001**, *18*, 691−699.
(56) Pattengale, N. D.; Alipour, M.; Bininda-Emonds, O. R. P.; Moret, B. M. E.; Stamatakis, A. How Many Bootstrap Replicates Are Necessary? *J. Comput. Biol.* **2010**, *17*, 337−354.
(57) Schmid, N.; Christ, C. D.; Christen, M.; Eichenberger, A. P.; Van Gunsteren, W. F. Architecture, Implementation and Parallelisation of the GROMOS Software for Biomolecular Simulation. *Comput. Phys. Commun.* **2012**, *183*, 890−903.
(58) Eichenberger, A. P.; Allison, J. R.; Dolenc, J.; Geerke, D. P.; Horta, B. A. C.; Meier, K.; Oostenbrink, C.; Schmid, N.; Steiner, D.; Wang, D.; van Gunsteren, W. F. GROMOS++ Software for the Analysis of Biomolecular Simulation Trajectories. *J. Chem. Theory Comput.* **2011**, *7*, 3379−3390.
(59) Berendsen, H. J. C.; Postma, J. P. M.; van Gunsteren, W. F.; Hermans, J. Interaction Models for Water in Relation to Protein Hydration. In *Intermolecular Forces. The Jerusalem Symposia on Quantum Chemistry and Biochemistry*; Pullman, B., Ed.; Springer: Dordrecht, The Netherlands, 1981; Vol. *14*, pp 331− 342.
(60) Tironi, I. G.; Sperb, R.; Smith, P. E.; Van Gunsteren, W. F. A Generalized Reaction Field Method for Molecular Dynamics Simulations. *J. Chem. Phys.* **1995**, *102*, 5451−5459.
(61) Berendsen, H. J. C.; Postma, J. P. M.; Van Gunsteren, W. F.; Dinola, A.; Haak, J. R. Molecular Dynamics with Coupling to an External Bath. *J. Chem. Phys.* **1984**, *81*, 3684−3690.
(62) Oliphant, T. *A guide to NumPy.*, 1st ed.; Trelgol Publishing, 2006.
(63) Hunter, J. D. Matplotlib: A 2D Graphics Environment. *Comput. Sci. Eng.* **2007**, *9*, 90−95.

https://dx.doi.org/10.1021/acscatal.0c00754
ACS Catal. 2020, 10, 4842−4853